Carbon nitride nanodots decorated brookite TiO_2 quasi nanocubes for enhanced activity and selectivity of visible-light-driven CO_2 reduction

Kan Li [1], Bosi Peng [1], Jingpeng Jin, Ling Zan, Tianyou Peng[*]

College of Chemistry and Molecular Sciences, Wuhan University, Wuhan 430072, PR China

ABSTRACT

A new kind of brookite TiO_2/g-C_3N_4 nanocomposite, in which g-C_3N_4 nanodots (CNDs) with a mean size of ~2.8 nm are decorated on brookite TiO_2 quasi nanocube (BTN) surfaces (hereafter referred as BTN-CNDs heterojunction), is prepared *via* a facile calcination process of the mixture of urea and the home-made BTN powders, and then used as visible-light-responsive photocatalyst for CO_2 reduction. Electron microscopy, X-ray powder diffraction (XRD), ultraviolet-visible light (UV-vis) diffuse reflectance absorption spectra (DRS), X-ray photoelectron spectra (XPS) and its valance band (VB) spectra are adopted to investigate the microstructure, composition, energy band structure, and the possible photogenerated electron transfer processes between BTN and CNDs. After optimizing the photocatalytic condition, enhanced visible-light-driven CO_2-reduction activity and selectivity for CH_4 generation as compared to g-C_3N_4 and BTN alone are observed, and a photosensitization mechanism is proposed to explain the differences in the photocatalytic performance among g-C_3N_4, BTN, and BTN-CNDs. The pronounced CH_4 generation activity and selectivity over BTN-CNDs heterojunction demonstrate a new strategy for improving the interfacial charge transfer and the photocatalytic CO_2 reduction performance though tailoring the microstructures of the semiconductor-based nanocomposites.

© 2016 Elsevier B.V. All rights reserved.

1. Introduction

Photocatalytic CO_2 reduction into chemical fuels (such as CO, CH_4, CH_3OH, C_2H_5OH, and so on) by utilizing solar energy over semiconducting materials is considered as a promising approach to solving the current energy pinch and global warming, which are of the most serious crises facing humanity [1–4]. Nowadays, various semiconductors such as metal oxides, sulfides, graphene-based materials and so on, are explored to act as CO_2-reduction photocatalysts [5–17]. Amongst those photocatalysts, TiO_2 is the most extensively investigated UV-light-responsive photocatalyst because of its exceptional properties such as high chemical stability, low cost, easy availability, and suitable band alignment to CO_2 reduction and water redox potentials [1–3,14]. Recently, it has been found that brookite TiO_2 with the most negative conductive band (CB) among the three TiO_2 polymorphs (anatase, brookite and rutile) [5,18–20], which leads to brookite having great potential in the field of photocatalytic CO_2 reduction. Nevertheless, brookite TiO_2 with a bandgap of ~3.20 eV only absorbs the UV light region

of the solar light [2,5,18–20], and thus coupling it with certain visible-light-responsive component is applied to expand the spectral responsive region [2,21].

Since Wang and co-workers [22] reported that graphitic carbon nitride (g-C_3N_4) displayed visible-light-driven activity, many efforts have been made to synthesize g-C_3N_4 with various morphologies and apply it in solar energy conversion [23–29]. Nevertheless, the photoactivity of the bare g-C_3N_4 is still limited due to the high recombination rate of the photogenerated carriers [23,26], and thus many strategies are developed to improve the photocatalytic performance of g-C_3N_4 [29,30]. On one hand, tailing the morphology of g-C_3N_4 can modify the activity. For example, g-C_3N_4 with a helical rod-like morphology (HR-CN) is synthesized by a nanocasting approach using chiral mesoporous silica (CMS) as the sacrificial template, and the multiple reflections of incident light and clipping carriers transfer along helical structure make ~20 folds enhancement in CO_2 to CO conversion rate than the bulk g-C_3N_4 [26]. On other hand, coupling g-C_3N_4 with wide bandgap semiconductor to form type II heterojunction may be another suitable approach to achieve a promoted charge separation and an improved CO_2 reduction activity, which originated from the well-aligned overlapping band structures of g-C_3N_4 and semiconductor [31–36]. Recently, a direct Z-scheme g-C_3N_4/ZnO composite with intimate interfacial contact has been prepared *via* a calcination pro-

cess utilizing urea and zinc nitrate hexahydrate as precursors [37]. Different from type II heterojunction in which g-C₃N₄ acts as electron donor [34–36], g-C₃N₄ as electron acceptor can promote the ZnO-to-g-C₃N₄ electron transfer at the interface, and thus resulting in a better CO_2 reduction activity than g-C₃N₄ alone [37].

Herein, a new kind of brookite TiO_2/g-C₃N₄ nanocomposite, in which g-C₃N₄ nanodots (CNDs) with a mean size of ~2.8 nm are uniformly decorated on brookite TiO_2 quasi nanocube (BTN) surfaces (hereafter referred as BTN-CNDs), is prepared *via* a facile calcination process of urea in the presence of the BTN powders derived from a hydrothermal process as reported previously [18]. The resultant BTN-CNDs heterojunction exhibits much better photocatalytic CO_2 reduction activity and selectivity for CH_4 generation than g-C₃N₄ and BTN alone under UV–vis or visible ($\lambda > 400$ nm) light irradiation. The effects of CNDs uniformly decorated on BTN surfaces on the charge separation processes and the photocatalytic CO_2 reduction performance are explored and elucidated with the aid of various characterization techniques, and a possible photosensitization mechanism, different from the direct Z-scheme g-C₃N₄/ZnO system reported previously [37], is proposed to explain the pronounced CH_4 generation activity and selectivity over the present BTN-CNDs nanocomposite.

2. Experimental

2.1. Material preparation

All reagents are of analytical grade and used as received without further purification. Brookite TiO_2 was prepared according to our previous reports [18]. Typically, $TiCl_4$ (2.85 g, ~15 mmol) was dropped into ice water (40 g). After the ice melted, urea (5.0 g) was added with continually stirring. Immediately following the urea dispersed, 5.0 mL of sodium lactate solution (~60%) was added drop wise, and then the mixture was transferred into a Teflon-lined autoclave (100 mL bulk volume), which was sealed and kept at 200 °C for 20 h, and then cooled to room temperature naturally. The precipitate was separated by centrifugation (10 k rpm) and washed with distilled water and absolute ethanol for several times, and then the product dried at 70 °C was calcined in air for 3 h at 500 °C with a heating rate of 2 °C min⁻¹.

Graphitic carbon nitride (g-C₃N₄) was synthesized by thermal treatment of urea in an alumina crucible with a cover [23]. The precursor was heated to 580 °C for 3 h at a heating rate of 10 °C min⁻¹. The yellow-colored product was washed with nitric acid (0.1 M) and distilled water to remove any residual alkaline species (e.g. ammonia) adsorbed on the sample surface, and then dried at 70 °C in vacuum overnight. The nanocomposite of g-C₃N₄ and brookite TiO_2 nanoparticles was also synthesized by thermal treatment. Typically, brookite TiO_2 nanoparticles (0.20 g) and urea (10.0 g, which is 50 folds of the brookite TiO_2) were uniformly grinding in the agate mortar, and then transferred into an alumina crucible with a cover, the mixture was heated to 580 °C for 3 h at a heating rate of 10 °C min⁻¹. The following wash methods were as the same as g-C₃N₄. If necessary, Pt-loaded sample was prepared through a photodeposition procedure. The obtained sample (0.20 g) was dispersed in 80 mL of deionized water in a photoreaction cell (Pyrex glass) containing 20 mL of methanol and H_2PtCl_6 solution under stirring, and then this mixture was irradiated using a 500 W high pressure Hg-lamp for 3 h under continuous magnetic stirring. After centrifugation, the sample was washed with water and dried at 70 °C overnight to obtain Pt-loaded sample.

2.2. Material characterization

X-ray powder diffraction (XRD) pattern was obtained by using Miniflex 600 X-ray diffractometer with Cu Kα irradiation ($\lambda = 0.154$ nm) at 40 kV and 15 mA. A scan rate of 4° min⁻¹ was applied to record the XRD pattern in the range of 2θ = 10°–50° with a step of 0.02°. The morphology was investigated with Zeiss-Sigma field emission scanning electron microscope (FESEM), and the high-resolution transmission electron microscopy (HRTEM) observation was conducted on a LaB₆ JEM-2100(HR) electron microscope (JEOL Ltd.) working at 200 kV. Nitrogen adsorption-desorption isotherms at 77 K were measured on a Micrometrics ASAP 2010 system after the samples were degassed at 120 °C. UV–vis diffuse reflectance absorption spectra (DRS) were obtained by a Shimadzu UV-3600 spectrophotometer equipped with an integrating sphere with $BaSO_4$ as the reference. The scan region was 800–200 nm with a step of 1 nm. X-ray photoelectron spectroscopy (XPS) measurement and XPS valance band (VB) spectra were performed on an ESCALAB 250Xi photoelectron spectroscope (Thermo Fisher Co.) equipped with a standard and monochromatic source (Al Kα).

In situ diffuse reflectance infrared Fourier transform spectra (DRIFTS) were recorded on a Nicolet iS50 spectrometer (Thermo Electron) equipped with a liquid nitrogen cooled HgCdTe (MCT/A) detector. The spectra in absorbance units, and acquired with a resolution of 4 cm⁻¹ by using 256 scans. Typically, photocatalyst (40 mg) was uniformly dispersed onto the DRIFTS accessory, which was thoroughly vacuum-treated to remove air completely, and then CO_2 (99.999%) and H_2O vapour were introduced into the reactor until 1 atm and then maintained for 20 min before collecting IR spectra. For obtaining the photocurrent-time curve, a working electrode (Pt wire) was immersed in 50 mL of suspension containing photocatalyst (25 mg) and NaOH (1.9 g). A saturated Ag/AgCl electrode and a Pt gauze electrode were used as reference and counter electrode, respectively. Before irradiation, the suspension was continuously purged by N_2 to remove O_2, and then illuminated by 300 W Xe-lamp. The working electrode was held at +0.5 V (*vs.* Ag/AgCl) by using a CHI618 workstation.

2.3. Photocatalytic activity measurement

CO_2 photoreduction was carried out in a home-made gas-closed circulation system operated under a 300 W Xe-lamp irradiation. In the CO_2-reduction system, photocatalyst (60 mg) was uniformly dispersed onto the watch-glass with an area of ~28 cm², which then put in 500 mL reaction cell (Pyrex glass). Before irradiation, the above system was thoroughly vacuum-treated to completely remove air. CO_2 and H_2O vapor were produced from the reaction of $NaHCO_3$ (1.50 g, introduced into the reactor before being sealed) and H_2SO_4 solution (5.0 mL, 4 M), which was introduced into the reactor *via* a syringe. During irradiation, 2 mL gas was taken from the reactor at regular intervals (1 h) for subsequent gas concentration analysis using a gas chromatograph (SP-7820, TDX-01 and GDX-502 columns, Rainbow chemical instrument Co., Ltd) equipped with a flame ionized detector (FID) and methanizer. The produced gases were calibrated with a standard gas mixture and their identity determined using the retention time. The corresponding overall activity for the CO/CH_4 generation can be estimated with total consumed electron number (TCEN), which can be calculated from the CO/CH_4 generation activity with Eq. (1) [5,17].

$$\text{TCEN} = \frac{2 \times (c_{\text{CO}} + 4c_{\text{CH}_4}) \times V_{\text{reactor}}}{m_{\text{cat.}} \times t_{\text{irr.}}}$$

Where, TCEN is the total consumed electron number for the CO/CH_4 generation. V_{reactor} is the reactor volume. $t_{\text{irr.}}$ is the irradiation time. $m_{\text{cat.}}$ is the catalyst mass. c_{CO} and c_{CH_4} are the produced CO and CH_4 concentration, respectively.
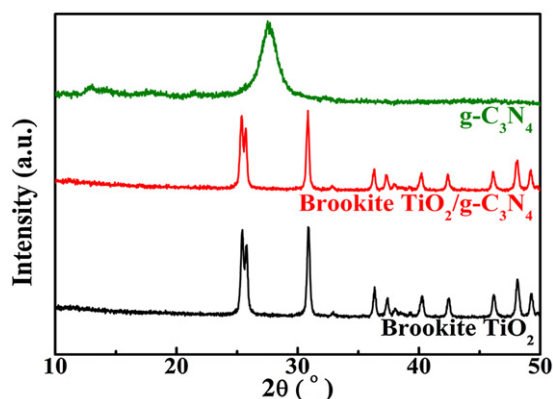
Fig. 1. X-ray powder diffraction (XRD) patterns of the obtained brookite TiO_2, g-C_3N_4, and brookite TiO_2/g-C_3N_4 nanocomposite.

3. Results and discussion

3.1. Crystal phase and microstructure analyses

Fig. 1 depicts the XRD patterns of the obtained brookite TiO_2, g-C_3N_4, and brookite TiO_2/g-C_3N_4 nanocomposite. As can be seen, the pristine brookite TiO_2 is well conformed to the orthorhombic brookite phase (JCPDS No. 65-2448) with diffraction peaks located at $2\theta = 25.3°$, $25.7°$, $30.8°$, $32.9°$, $36.2°$, $37.3°$, $40.1°$, $42.4°$, $46.0°$, $48.0°$, and $49.1°$, which can be attributed to the reflections of (210), (111), (211), (020), (102), (021), (202), (221), (302), (321), and (312) planes [5], respectively. Also, the high phase purity of the present brookite TiO_2 is in well agreement with our previous works [5,18]. The pristine g-C_3N_4 shows two broad diffraction peaks at $2\theta = {\sim}13°$ and $27°$, which are related to the reflections of its (100) and (002) planes that can be ascribed to the characteristic inter-layer structural packing and the interplanar stacking peaks of the aromatic systems, respectively [23,37]. Nevertheless, no any evident XRD peak related to the characteristic interlayer structural packing and interplanar stacking of g-C_3N_4 can be observed from the brookite TiO_2/g-C_3N_4 nanocomposite, indicating the low content and well dispersion of g-C_3N_4 species on the brookite TiO_2 particle surfaces as mentioned below.

Fig. 2 shows the typical FESEM images of the obtained brookite TiO_2 and brookite TiO_2/g-C_3N_4 nanocomposite. As can be seen from Fig. 2a, the pristine brookite TiO_2 nanoparticles have quasi nanocube-like morphology with smooth surfaces. The particle sizes are distributed in the range of 15–84 nm with a mean size of ~50 nm, which is in well agreement to our previous works [5,18]. After the calcination process of urea, the quasi nanocube-like morphology of brookite TiO_2 nanoparticles can be maintained, and no obvious surface change can be observed from the brookite TiO_2/g-C_3N_4 nanocomposite (Fig. 2b). TEM image (Fig. 3a) displays that

the obtained brookite TiO_2 particles exhibit quasi nanocube-like morphology with smooth surfaces and sharp edges, which are consistent with our previous report [18]. The lattice fringes of the HRTEM image and the corresponding fast Fourier transform (FFT) pattern (Fig. 3b and its inset) indicate the brookite TiO_2 quasi nanocubes (hereafter denoted as BTN) are mainly surrounded with {210} facets with an interfacial angle between (210) and (2–10) facets consistent well with the theoretical value (~80°), and the top/bottom sides of nanocube are perpendicular to the incident beam (parallel to [001] direction) [5,18]. After the calcination process of urea, many g-C_3N_4 nanodots (hereafter denoted as CNDs) are uniformly decorated on each facets of BTN particle (denoted as BTN-CNDs), and the CNDs' sizes are in the range of 1.1–3.8 nm centered at ~2.8 nm (Fig. 3c and its inset). The HRTEM image (Fig. 3d) of BTN-CNDs indicates that the BTN particle is surrounded by those small sized CNDs to form BTN-CNDs heterojunction, and the denoted lattice fringes with a d-spacing of 0.325 nm for the decorated CND corresponds well to the (002) plane of g-C_3N_4 [38]. The intimate contact interfaces (Fig. 3d) between the BTN particle and CNDs would enhance the charge transfer and separation between the two phases, and thus resulting in an enhanced photoactivity of the BTN-CNDs heterojunction.

Nitrogen adsorption-desorption experiments indicate that the obtained BTN-CNDs exhibits a typical type III isotherm with H3 hysteresis loop, which is similar to the pristine BTN but with a decrease in the Brunauer-Emmett-Teller (BET) specific surface area (S_{BET}) from 42.2 to 32.6 $m^2 g^{-1}$ (Fig. 4a). Also, the CNDs-loading leads to a decrease in the mean pore size (from 30 to 19.7 nm) with the pore volume dropped by ~27% as can be observed from the Barret-Joyner-Halenda (BJH) pore size distribution plots (Fig. 4b), and thus the S_{BET} decrease after the CNDs-loading on BTN can be related to those changes in pore volume and pore size synergistically [34–36].

3.2. Optical property and energy band structure analyses

Fig. 5 depicts the UV–vis diffuse reflectance absorption spectra (DRS) of the obtained g-C_3N_4, BTN and BTN-CNDs. As can be seen, the pristine g-C_3N_4 and BTN present an onset absorption edges at ~446 nm and ~382 nm, corresponding to a bandgap of ~2.78 and ~3.25 eV [18,23,26,37], respectively. The BTN-CNDs nanocomposite shows an enhanced visible absorption in the region of 400–500 nm with an absorption edge similar to that of g-C_3N_4, which might be beneficial for extending the visible-light-responsive region of BTN for the photocatalytic CO_2 conversion.

X-ray photoelectron spectra (XPS) exhibit that BTN-CNDs are mainly composed of Ti 2p, O 1s, N 1s, and C 1s binding energy peaks (Fig. S1a, ESI†), and the Ti 2p spectrum (Fig. S1b, shows two symmetric peaks at 458.3 and 464.1 eV), which can be ascribed to electron binding energy of Ti $2p_{3/2}$ and $2p_{1/2}$, respectively. The Ti 2p spectrum of BTN decorated with C_3N_4 nanodots exhibits peak positions very similar to that reported previously [39], confirming the
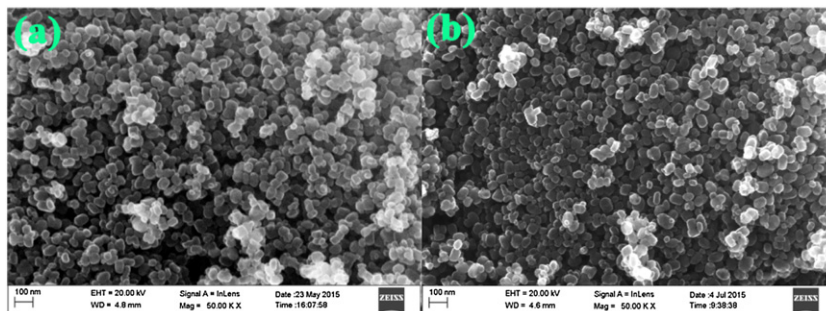
Fig. 2. Typical FESEM images of the obtained brookite TiO_2 (a) and brookite TiO_2/g-C_3N_4 nanocomposite (b).
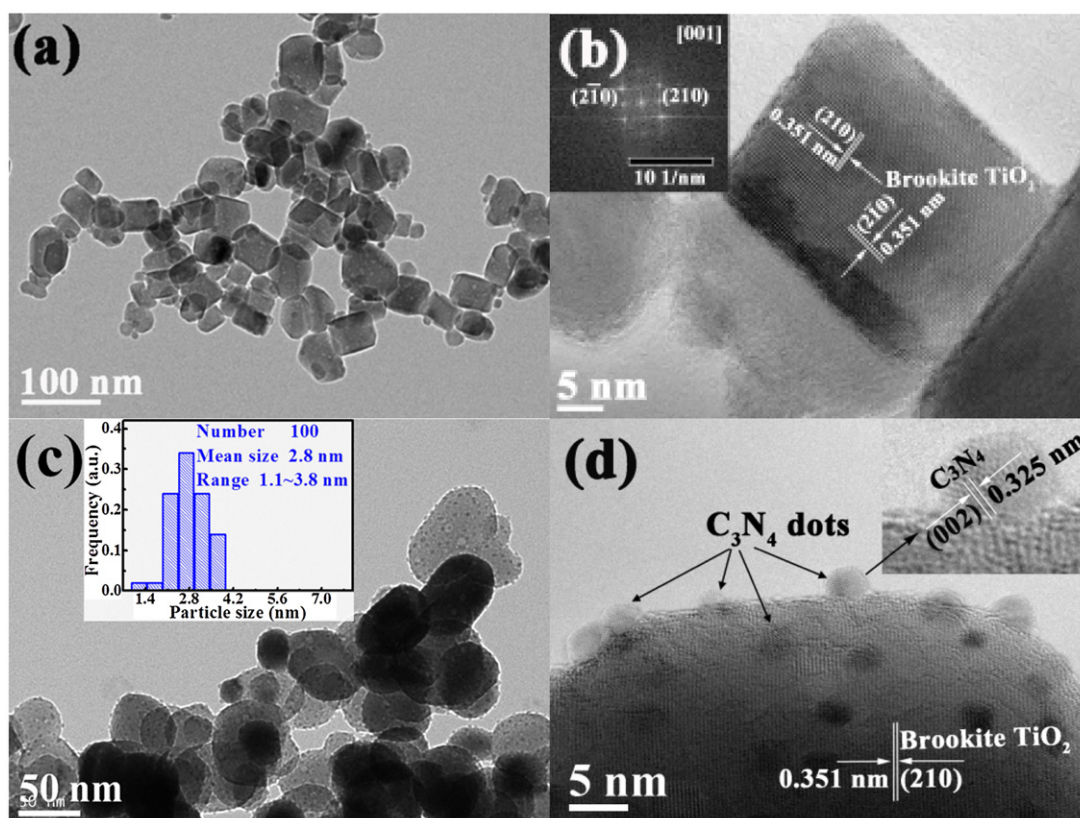
Fig. 3. Typical TEM and HRTEM images of the obtained BTN (a, b) and BTN-CNDs (c, d).
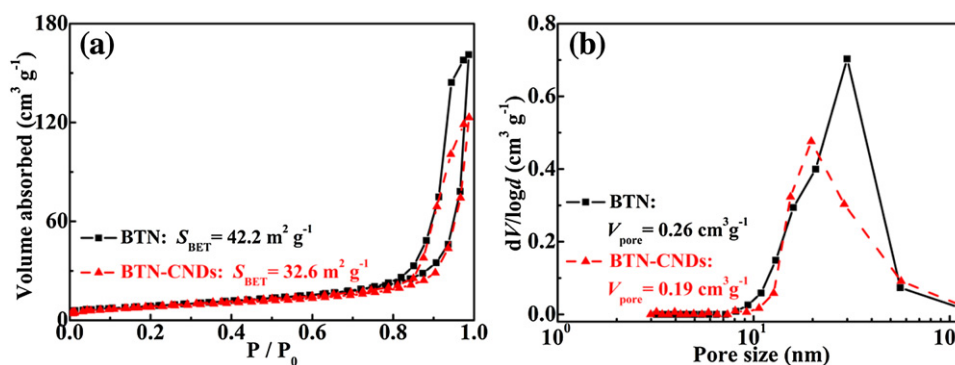

Fig. 4. Nitrogen adsorption-desorption isotherms (a) and Barret-Joyner-Halenda (BJH) pore size distribution plots (b) of the obtained BTN and BTN-CNDs.

stability of BTN particles during the urea calcination process. The high resolution C 1 s spectra (Fig. S1c) of BTN-CNDs can be deconvolved into three peaks at 288.4, 286.4, and 284.6 eV, corresponding to sp^2-bonded carbon (N—C=N), C—O and graphite carbon (C—C) bonds [23,26,40], respectively. The evdient C—O intensity hints a good CO_2 adsorption capability on BTN-CNDs [23,26]. Also, the N 1s spectra (Fig. S1d) can be mainly fitted with three peaks at 401.2, 399.6, and 398.7 eV, corresponding to N—H side groups, tertiary N bonded to carbon atoms ((C)$_3$—N), and sp^2 hybridized aromatic N bonded to carbon atoms (C=N—C) of g-C_3N_4 [8,26], respectively. Moreover, BTN-CNDs show O 1 s binding energy peaks at 529.8 eV and 531.2 eV (Fig. S1e), related to the Ti—O bonds and the hydroxyl (O—H) groups adsorbed on the BTN surfaces [5], respectively. The above XPS spectra verify the bond structures of g-C_3N_4 species in BTN-CNDs, while the XPS valance band (VB) spectra can give the information on energy band structures of BTN-CNDs [41,42]. As can be seen from the XPS VB spectra (Fig. S1f), the pristine g-C_3N_4 and

BTN has a VB edge of ∼1.30 and ∼2.40 eV, respectively. Whereas the BTN-CNDs shows a VB edge similar to the brookite TiO_2, possibly due to the high dispersion of those small sized g-C_3N_4 nanodots on BTN surfaces.

3.3. Photocatalytic CO_2 reduction activity analyses

Control experiments showed no appreciable reduced C1/C2 product detected in the absence of either photocatalyst or irradiation, implying that both photocatalyst and irradiation are necessary for the present gaseous CO_2 photoreduction system. Also, a contrast test in the absence of CO_2 but in the presence of H_2O and photocatalyst showed no appreciable reduced C1/C2 product, confirming that the origin of the carbon-containing products from the present photoreaction system are derived from CO_2 rather than from the possible organic impurities either the organics involved in the synthesis or the organic solvents existed in laboratory atmosphere that
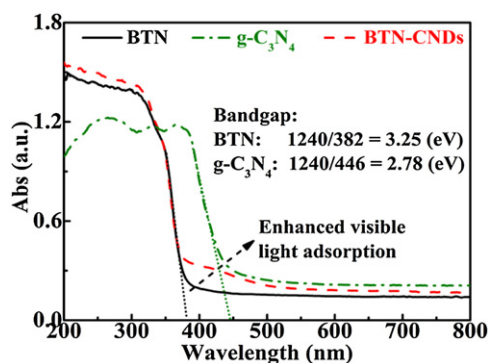
Fig. 5. UV–vis diffuse reflectance absorption spectra (DRS) of the obtained g-C$_3$N$_4$, BTN, and BTN-CNDs.

could be adsorbed on the catalyst surface. Fig. 6 depict the photocatalytic CO$_2$ reduction activity of the obtained BTN, g-C$_3$N$_4$ and BTN-CNDs under an initial 2 h of light irradiation. The CO/CH$_4$ generation rates of BTN are 0.74/0.17 μmol g^{-1} h^{-1} under visible light ($\lambda > 400$ nm) irradiation (Fig. 6a); while the corresponding data are 3.31/0.73 μmol g^{-1} h^{-1} under UV–vis light (Xe-lamp full spectrum) irradiation (Fig. 6b). Namely, the pristine BTN exhibits selective generation of CO as compared to CH$_4$ under both illumination situations.

Although g-C$_3$N$_4$ also exhibits a similar selectivity for CO generation, there are obvious differences in activity and selectivity for the generation of CO/CH$_4$ over BTN-CNDs under both illumination situations. For instance, the CH$_4$ generation rate of BTN-CNDs significantly increases from 0.17 to 5.21 μmol g^{-1} h^{-1} with CO generation rate slightly enhanced from 0.74 to 0.84 μmol g^{-1} h^{-1} under visible light irradiation. In addition, the CH$_4$ generation rate of BTN-CNDs under visible light is also ~2.9 times of g-C$_3$N$_4$ alone. It indicates that g-C$_3$N$_4$ nanodots decorated on BTN particles can achieve a much better selectivity for CH$_4$ generation than the BTN and g-C$_3$N$_4$ alone.

The overall activity for CO/CH$_4$ generation can be estimated with total consumed electron number (TCEN), which is calculated from the CO/CH$_4$ generation rates [5,17]. As shown in Fig. 6, the overall activities (TCEN values) of BTN-CNDs under visible and UV–vis light irradiations are 43.4 and 58.1 μmol g^{-1} h^{-1}, which is ~15.0 and ~4.6 times of BTN alone, respectively. This result indicates that BTN-CNDs exhibits much better overall activity than g-C$_3$N$_4$ and BTN alone. By using visible light instead of UV–vis light, the pristine BTN shows a significant decrease (~76.8%) in the overall activity, while g-C$_3$N$_4$ and BTN-CNDs exhibit much smaller decreases (25.9% for g-C$_3$N$_4$, and 25.3% for BTN-CNDs). It indicates that g-C$_3$N$_4$ nanodots on BTN particles can improve the visible-light-driven CO$_2$ reduction activity, which is mostly related to the photosensitization of g-C$_3$N$_4$ species. Since the CB edge potential ($E_{CB} = -1.10$ V

vs. NHE [43]) of g-C$_3$N$_4$ is more negative than that ($E_{CB} = -0.50$ V vs. NHE [5,18]) of brookite TiO$_2$, the thus a fast g-C$_3$N$_4$-to-BTN electron transfer via the intimate interfacial contact is allowed thermodynamically.

Also, Fig. 6a shows that the TCEN value (43.4 μmol g^{-1} h^{-1}) of BTN-CNDs under visible light illumination are much higher than the corresponding TCEN summation (31.5 μmol g^{-1} h^{-1}) of the pristine BTN (2.9 μmol g^{-1} h^{-1}) and g-C$_3$N$_4$ (28.6 μmol g^{-1} h^{-1}). Similarly, BTN-CNDs under UV–vis light illumination exhibits a TCEN value of 58.1 μmol g^{-1} h^{-1}, also higher than the corresponding TCEN summation (51.1 μmol g^{-1} h^{-1}) of the pristine BTN (12.5 μmol g^{-1} h^{-1}) and g-C$_3$N$_4$ (38.6 μmol g^{-1} h^{-1}) as shown in Fig. 6b. This result implies an evident synergistic effect between the g-C$_3$N$_4$ nanodots and the brookite TiO$_2$ particles in the present BTN-CNDs under both illumination situations. To further comprehend this issue, various Pt-loaded samples with different loading positions are prepared. First of all, the effect of Pt-loading amount on the photocatalytic CO/CH$_4$ generation rates over BTN under UV–vis light irradiation was measured, and the corresponding results were shown in Fig. S2. As can be seen, the optimal Pt-loading amount for CO$_2$ reduction over BTN (Pt-BTN) under UV–vis light illumination is 0.75 wt%, and thus the Pt-loading amount was maintained at this level for investigating the effect of Pt-loading position on the photocatalytic performance of BTN-CNDs.

As shown in Fig. 7, the overall CO$_2$ reduction activity (110.6 μmol g^{-1} h^{-1} under visible light) of 0.75 wt% Pt-BTN after calcination at 580 °C (as the preparation process of BTN-CNDs but without addition of urea) is more than 38 times as high as the pristine BTN (2.9 μmol g^{-1} h^{-1} under visible light, ref. Fig. 6a). Generally, this extremely enhamcement in overall CO$_2$ reduction activity can be ascribed to the enhanced selectivity of CH$_4$ formation and the more efficient charge separation due to the loaded Pt nanoparticles acting as electron sinks. On one hand, the enrichment of electron density on Pt nanoparticles can enhance the probability of multielectron reactions to CH$_4$ formation, while CO was formed as a major product over BTN (ref. Fig. 6) possibly because of the low density of electrons [44]. On the other hand, the formation of CH$_4$ requies eight electrons, while that of CO only needs two electrons, and thus the enhanced selectivity of CH$_4$ formation is more efficient for improving the overall CO$_2$ reduction activity since it was calculated from the total consumed electron number according to Eq. (1).

Similarly, the overall CO$_2$ reduction activity of BTN-CNDs under visible light can also be significantly improved by Pt-loading as shwon in Fig. 7. For instance, (Pt-BTN)-CNDs derived from the urea calcination process by using Pt-BTN as the substrate achieved an overall activity (244.6 μmol g^{-1} h^{-1}), which is slightly lower than that (261.8 μmol g^{-1} h^{-1}) of Pt-(BTN-CNDs) derived from the Pt-loading process by using BTN-CNDs as the substrate. Both of them are much higher than that (43.4 μmol g^{-1} h^{-1}) of BTN-CNDs

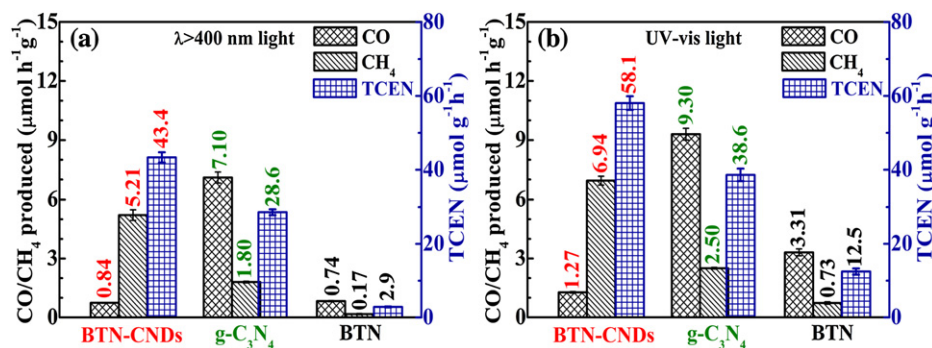**Fig. 6.** Photocatalytic CO$_2$ reduction activity and selectivity of the obtained g-C$_3$N$_4$, BTN, and BTN-CNDs during the initial 2 h of visible (a) and UV–vis (b) light irradiation.
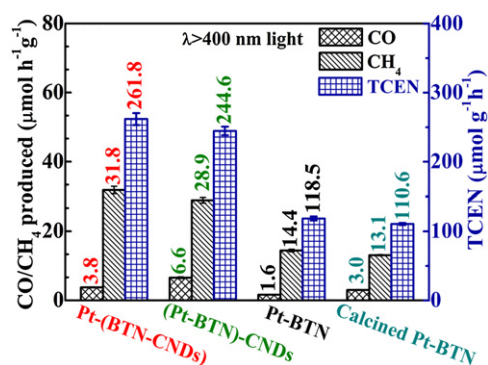
Fig. 7. Photocatalytic CO_2 reduction activity of various Pt-loaded samples during the initial 2 h of visible light irradiation.
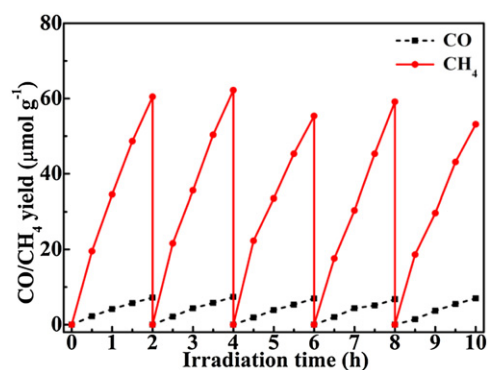

Fig. 8. Typical time course for the photocatalytic CO/CH_4 generation over Pt-(BT-CNDs) under visible light irradiation.
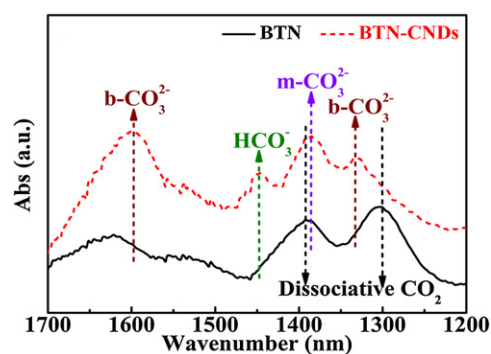

Fig. 9. *In situ* DRIFT IR spectra of CO_2 interaction with the obtained BTN and BTN-CNDs.

Fig. 10. The probable mechanisms of the photocatalytic CO/CH_4 generation over Pt-loaded BTN-CNDs.

(Fig. 6a). It can be due to the similar Pt distributions on BTN surfaces in the two samples since only very small sized CNDs spread on BTN surfaces, while the possible reason for the slightly higher photoactivity of Pt-(BTN-CNDs) than (Pt-BTN)-CNDs is that more Pt nanoparticles grafted *via* the present photodeposition process might be located around the CNDs in Pt-(BTN-CNDs) compared to (Pt-BTN)-CNDs [45]. Furthermore, the typical time courses (Fig. 8) for CO/CH_4 generation over Pt-(BTN-CNDs) exhibit no obvious decrease in both activity and selectivity for CO/CH_4 generation during 10 h irradiation, verifying the well stability of those g-C_3N_4 nanodots decorated on BTN surfaces.

In addition, CO_2 adsorption amount and existing state are also affected by those g-C_3N_4 nanodots decorated on BTN particles as shown in the *in situ* DRFIT IR spectra (Fig. 9). The pristine BTN exhibits stronger peaks at ~1300/1392 cm^{-1} ascribable to the dissociative CO_2, implying the poor CO_2 adsorption capability of BTN alone [46]. After decorated with g-C_3N_4 nanodots on BTN particles, monodentat carbonate (m-CO_3^{2-}, 1387 cm^{-1}), bidentate carbonate (b-CO_3^{2-}, 1332/1597 cm^{-1}) and bicarbonate (HCO_3^-, 1446 cm^{-1}) [46–48] are formed on BTN-CNDs due to the introduction of alkaline sites of N-atoms [26,34–36], suggesting the better adsorptions of carbonates and/or its hydrolytes, which can promote the photocatalytic CO_2 reduction reactions.

Based on the above discussion on the light absorption and -OH/CO_2 adsorption, a photosensitization mechanism is proposed to explain the significantly enhanced visible-light-driven CO_2-reduction activity over BTN-CNDs as shown in Fig. 10. Under visible light irradiation, most photoinduced electrons of g-C_3N_4 nanodots can directionally migrate and inject into BTN thermodynamically, which then convert CO_2 into CO/CH_4 on BTN surfaces (solid lines in Fig. 10). Also, a small amount of photoinduced electrons can convert CO_2 into CO/CH_4 on those g-C_3N_4 nanodots. Since very small sized
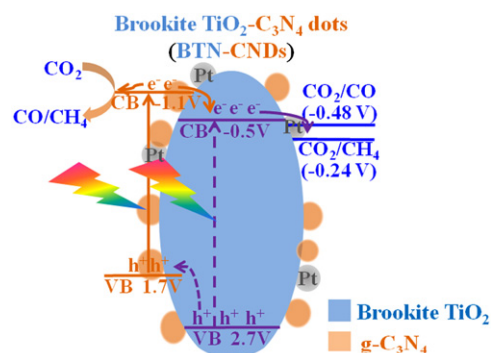
g-C_3N_4 nanodots spread on BTN particle surfaces for BTN-CNDs, the loaded Pt nanoparticles would mainly locate on BTN particle surfaces, and act as electron sinks to further promote the CNDs-to-BTN electron transfer, and then to improve the photocatalytic CO_2 reduction performance. Under UV–vis light irradiation, BTN particles in BTN-CNDs can also be excited, and thus causing the enhanced activity (dash lines in Fig. 10) as compared to the g-C_3N_4 alone under visible light irradiation.

The above results indicate that the present BTN-CNDs has better charge separation efficiency and CO_2 reduction activity than BTN alone, which can be validated by the photocurrent responses (*J-t* curves) of photocatalyst suspension (Fig. S3). Also, BTN-CNDs under UV–vis light can be considered as a type II heterojunction (but not a Z-scheme system as ZnO/g-C_3N_4 mentioned above [37]) since the photoinduced electrons of g-C_3N_4 nanodots can inject into CB of BTN particles, and the holes of the photoexcited BTN can hop into the VB of g-C_3N_4 (Fig. 10), which is beneficial for the charge carriers separation in space, and thus leads to the enhancement of activity of BTN-CNDs as compared to BTN or g-C_3N_4 alone. Although the photogenerated electrons can be mainly consumed through the reduction of CO_2 and H_2O into CO and CH_4 as mentioned above, no obvious oxidative product such as O_2 that possibly induced by the positive-charged holes was detected in the present photoreaction system by GC. Nevertheless, it was found that the CO and CH_4 production was sustainable as shown in Fig. 8. It implies that some other oxidative product other than O_2 should be produced during the present photocatalytic system. Recently, Ye's group has also found that there was no O_2 evolving in a Rh/Au loaded $SrTiO_3$ system for a photoreaction of CO_2 reduction, and further demonstrated the generated O_2 stop at the status of surface adsorbed •O_2^- (a form of −Ti−O−O−Ti−) through XPS measurements [49]. Possibly, the oxidative product in our CO_2 photoreduction system

also existed as a similar surface adsorbed $\cdot O_2^-$ species, which need further investigation.

The pronounced selectivity for CH_4 generation over BTN-CNDs in various situations (*i.e.* with or without Pt loading) as mentioned above can be attributed to a synergistic effect as follows: (1) uniform distribution of those small sized g-C_3N_4 nanodots on BTN surfaces can introduce more defect states in the g-C_3N_4 phase and large exposed brookite TO_2 particle surface for the adsorption of reactants for CO_2 reduction; (2) well-aligned overlapping band structures and intimate interfacial contacts among the brookite TiO_2 particle and those g-C_3N_4 nanodots lead to efficiently oriented electron transfer alone CNDs-to-BTN, which is beneficial for enhancing the surface electron density on BTN particles, and then for the more complex multi-electron CH_4 generation reaction; (3) the better adsorptions of hydroxyl and bicarbonate on BTN-CNDs than BTN alone introduce extra protons necessary for the CH_4 generation reaction.

4. Conclusion

In summary, a new kind of brookite TiO_2/g-C_3N_4 nanocomposite, in which g-C_3N_4 nanodots (CNDs) with a mean size of ∼2.8 nm are decorated on brookite TiO_2 quasi nanocube (BTN) surfaces to for BTN-CNDs heterojunction, is prepared *via* a facile calcination process of urea in the presence of the home-meade BTN powder. It is found that the resultant BTN-CNDs heterojunction exhibits a much better CO_2 reduction activity and selectivity for CH_4 generation than g-C_3N_4 and BTN alone. A photosensitization mechanism is proposed to explain the differences in the visible-light-driven photocatalytic performance among g-C_3N_4, BTN and BTN-CNDs, and the pronounced CO_2 reduction selectivity for CH_4 generation of BTN-CNDs as compared to g-C_3N_4 and BTN alone can be attributed to the synergistic effect as follows: (1) uniform distribution of those small sized g-C_3N_4 nanodots on BTN surfaces introduce better adsorption capacity of reactants for CO_2 reduction; (2) well-aligned overlapping band structures and intimate contacts promote the oriented electron transfer alone CNDs-to-BTN and the more complex multi-electron CH_4 generation reaction, (3) better hydroxyl/carbonate adsorption on BTN-CNDs than BTN alone introduces extra protons necessary for the CH_4 generation reaction. The present study provides a new route for the efficient separation of the charge carriers and the improvement of the CO_2 reduction activity and selectivity for CH_4 generation though tailoring the morphology and microstructures of composite photocatalysts.

Acknowledgments

Appendix A. Supplementary data

Supplementary data associated with this article can be found, in the online version, at http://dx.doi.org/10.1016/j.apcatb.2016.11.001.

References

[1] T. Inoue, A. Fujishima, S. Konishi, K. Honda, Nature 277 (1979) 637–638.
[2] S.N. Habisreutinger, L. Schmidt-Mende, J.K. Stolarczyk, Angew. Chem. Int. Ed. 52 (2013) 7372–7408.
[3] J. Mao, K. Li, T.Y. Peng, Catal. Sci. Technol. 3 (2013) 2481–2498.
[4] L. Yuan, Y.J. Xu, Appl. Surf. Sci. 342 (2015) 154–167.
[5] K. Li, T.Y. Peng, Z.H. Ying, S.S. Song, J. Zhang, J. Appl. Catal. B 180 (2016) 130–138.
[6] L.Q. Ye, J. Mao, T.Y. Peng, L. Zan, Y.Z. Zhang, Phys. Chem. Chem. Phys. 16 (2014) 15675–15680.
[7] J. Mao, T.Y. Peng, X.H. Zhang, K. Li, L. Zan, Catal. Commun. 28 (2012) 38–41.
[8] P. Li, Y. Zhou, Z.Y. Zhao, Q.F. Xu, X.Y. Wang, M. Xiao, Z.G. Zou, J. Am. Chem. Soc. 137 (2015) 9547–9550.
[9] T. Baran, S. Wojtyla, A. Dibenedetto, M. Aresta, W. Macyk, Appl. Catal. B 178 (2015) 170–176.
[10] J.S. Chen, S.Y. Qin, G.X. Song, T.Y. Xiang, F. Xin, X.H. Yin, Dalton Trans. 42 (2013) 15133–15138.
[11] R.K. Yadav, J.O. Baeg, A. Kumar, K.J. Kong, G.H. Oh, N.J. Park, J. Mater. Chem. A 2 (2014) 5068–5076.
[12] I. Shown, H.C. Hsu, Y.C. Chang, C.H. Lin, P.K. Roy, A. Ganguly, C.H. Wang, J.K. Chang, C.I. Wu, L.C. Chen, K.H. Chen, Nano Lett. 14 (2014) 6097–6103.
[13] H.C. Hsu, I. Shown, H.Y. Wei, Y.C. Chang, H.Y. Du, Y.G. Lin, C.A. Tseng, C.H. Wang, L.C. Chen, Y.C. Lin, K.H. Chen, Nanoscale 5 (2013) 262–268.
[14] W.K. Li, X.Q. Gong, G.Z. Lu, A. Selloni, J. Phys. Chem. C 112 (2008) 6594–6596.
[15] F.L. Wang, J.H. Ho, Y.J. Jiang, R. Amal, ACS Appl. Mater. Interfaces 7 (2015) 23941–23945.
[16] J.B. Priebe, J. Radnik, A.J.J. Lennox, M.M. Pohl, M. Karnahl, D. Hollmann, K. Grabow, U. Bentrup, H. Junge, M. Beller, A. Bruckner, ACS Catal. 5 (2015) 2137–2148.
[17] K. Li, L. Lin, T.Y. Peng, Y.Y. Guo, R.J. Li, J. Zhang, Chem. Commun. 51 (2015) 12443–12446.
[18] J.L. Xu, K. Li, S.F. Wu, W.Y. Shi, T.Y. Peng, J. Mater. Chem. A 3 (2015) 7453–7462.
[19] H. Lin, L.P. Li, M.L. Zhao, X.S. Huang, X.M. Chen, G.S. Li, R.C. Yu, J. Am. Chem. Soc. 134 (2012) 8328–8331.
[20] M. Zhao, H. Xu, H.R. Chen, S.X. Ouyang, N. Umezawa, D.F. Wang, J.H. Ye, J. Mater. Chem. A 3 (2015) 2331–2337.
[21] O. Ola, M.M. Maroto-Valer, J. Photochem. Photobiol. C 24 (2015) 16–42.
[22] X.C. Wang, K. Maeda, A. Thomas, K. Takanabe, G. Xin, J.M. Carlsson, K. Domen, M. Antonietti, Nat. Mater. 8 (2009) 76–80.
[23] J. Mao, T.Y. Peng, X.H. Zhang, K. Li, L.Q. Ye, L. Zan, Catal. Sci. Technol. 3 (2013) 1253–1260.
[24] J.L. Lin, Z.M. Pan, X.C. Wang, ACS Sustain. Chem. Eng. 2 (2014) 353–358.
[25] W.J. Ong, L.L. Tan, S.P. Chai, S.T. Yong, Chem. Commun. 51 (2015) 858–861.
[26] Y. Zheng, L.H. Lin, X.J. Ye, F.S. Guo, X.C. Wang, Angew. Chem. Int. Ed. 53 (2014) 11926–11930.
[27] G.G. Zhang, C.J. Huang, X.C. Wang, Small 11 (2015) 1215–1221.
[28] S. Ye, R. Wang, M.Z. Wu, Y.P. Yuan, Appl. Surf. Sci. 358 (2015) 15–27.
[29] Q. Huang, J.G. Yu, S.W. Cao, C. Cui, B. Cheng, Appl. Surf. Sci. 358 (2015) 350–355.
[30] K. Wang, Q. Li, B.S. Liu, B. Cheng, W.K. Ho, J.G. Yu, Appl. Catal. B Environ. 176–177 (2015) 44–52.
[31] W.J. Ong, L.K. Putri, L.L. Tan, S.P. Chai, S.Y. Yong, Appl. Catal. B 180 (2016) 530–543.
[32] S. Zhou, Y. Liu, J.M. Li, Y.J. Wang, G.Y. Jiang, Z. Zhao, D.X. Wang, A.J. Duan, L. Liu, Y.C. Wei, Appl. Catal. B 158 (2014) 20–29.
[33] S.W. Cao, X.F. Liu, Y.P. Yuan, Z.Y. Zhang, Y.S. Liao, J. Fang, S.C.J. Loo, T.C. Sum, C. Xue, Appl. Catal. B 147 (2014) 940–946.
[34] J.G. Yu, K. Wang, W. Xiao, B. Cheng, Phys. Chem. Chem. Phys. 16 (2014) 11492–11501.
[35] H.F. Shi, G.Q. Chen, C.L. Zhang, Z.G. Zou, ACS Catal. 4 (2014) 3637–3643.
[36] Y.M. He, Y. Wang, L.H. Zhang, B.T. Teng, M.H. Fan, Appl. Catal. B 168 (2015) 1–8.
[37] W.L. Yu, D.F. Xu, T.Y. Peng, J. Mater. Chem. A 3 (2015) 19936–19947.
[38] W.J. Ong, L.L. Tan, S.P. Chai, S.T. Yong, A.R. Mohamed, Nano Energy 13 (2015) 757–770.
[39] B. Chai, T.Y. Peng, P. Zeng, J. Mao, J. Mater. Chem. 21 (2011) 14587–14593.
[40] Z. Zhang, D. Jiang, D. Li, M. He, M. Chen, Appl. Catal. B 183 (2016) 113–123.
[41] X. Chen, L. Liu, F. Huang, Chem. Soc. Rev. 44 (2015) 1861–1885.
[42] X.B. Chen, L. Liu, P.Y. Yu, S.S. Mao, Science 331 (2011) 746–750.
[43] X.H. Zhang, T.Y. Peng, L.J. Yu, R.J. Li, Q.Q. Li, Z. Li, ACS Catal. 5 (2015) 504–510.
[44] S.J. Xie, Y. Wang, Q.H. Zhang, W.P. Deng, Y. Wang, ACS Catal. 4 (2014) 3644–3653.
[45] T. Kawahara, Y. Konishi, H. Tada, N. Tohge, J. Nishii, S. Ito, Angew. Chem. Int. Ed. 41 (2002) 2811–2813.
[46] L. Liu, H. Zhao, J.M. Andino, Y. Li, ACS Catal. 2 (2012) 1817–1828.
[47] H. He, P. Zapol, L.A. Curtiss, J. Phys. Chem. C 114 (2010) 21474–21481.
[48] J. Mao, L.Q. Ye, K. Li, X.H. Zhang, J.Y. Liu, T.Y. Peng, L. Zan, Appl. Catal. B 144 (2014) 855–862.
[49] D.W. Li, S.X. Ouyang, H. Xu, D. Lu, M. Zhao, X.L. Zhang, J.H. Ye, Chem. Commun. 52 (2016) 5989–5992.